The Composite Horizontal Wind Field within Convective Structures of the Atmospheric Surface Layer

E. P. WEIJERS,*,# A. VAN DELDEN,† H. F. VUGTS,* AND A. G. C. A. MEESTERS*

*Department of Meteorology, Vrije Universiteit, Amsterdam, The Netherlands
†Institute for Marine and Atmospheric Research, Utrecht University, Utrecht, The Netherlands

ABSTRACT

The horizontal perturbation wind field within thermal structures encountered in the atmospheric surface layer was investigated. A field experiment with four sonic anemometers on the vertices and one in the centroid of a square (with sides of 80 m) was performed to obtain the necessary dataset. Structures were selected on a typical ramplike appearance in the temperature time series. Ultimately, a set of 47 "ramps" was obtained. Conditional sampling and block averaging followed by a compositing technique were applied to construct ensemble averages of turbulent temperature and horizontal and vertical velocity. Properties of the horizontal velocity field were expressed in terms of ensemble averages of horizontal divergence, vertical vorticity, and deformation.

The ensemble-averaged behavior at the five masts during passage of thermal activity was consistent. The convergent wind field within a ramp attains its maximum simultaneously with the maximum in vertical velocity. Both precede the temperature extreme. The air in the ramp is clearly decelerated, while it is accelerated in the succeeding downdraft. In the frame of reference moving with the ramp the average orientation of the wind vector in the accompanying downdrafts is always directed toward the position of the ramp. Within the ramp, dilatation of air is measured in the direction of the mean wind. Near the microfront, contraction of air occurs with a maximum in the succeeding downdraft. Vertical vorticity (of opposite sign) is measured in the right and left half of the ramps. Phenomena involved in the generation of this vorticity are discussed. The strength of the background wind might play a role in the generation of these rotations.

1. Introduction

This paper presents measurements of horizontal flow fields in and around turbulent structures encountered in the surface layer (SL) of a convective atmosphere. The study is limited to structures that can be recognized by a typical ramplike shape in the time series of temperature (Antonia and Chambers 1978): during their passage a slow increase is followed by a sharp drop at the upwind edge (the edge that is seen last by a stationary observer). They are further characterized by net upward velocities and alternated by periods with downward movements of relatively quiescent cooler air. In literature, this thermal activity is usually referred to as "ramp" or "plume." The rapid horizontal temperature change at the upwind edge is called "microfront."

A concise review of properties is now given as far as these are relevant here. Usually a ramp can be observed almost simultaneously at all levels in the SL (Taylor 1958; Kaimal and Businger 1970; Kaimal 1974; Wilczak and Tillman 1980). The structure is tilted in the downwind direction. Summarizing the experimental findings of various authors, Antonia et al. (1979) estimated an average inclination angle of 45°; the range was considerable: 26°–65°.

Plumes propagate in the direction of the surface wind (Davison 1974). The determination of their translation velocity is still a matter of controversy. Wilczak (1984), considering the contradictory results of several experiments, suggested that the translation velocity of ramps is probably 70%–80% of the mean boundary-layer wind speed. It may vary from ramp to ramp in proportion to the plume height (Wilczak and Tillman 1980).

Plumes are elongated longitudinally (Phong-Anant et al. 1981) under the influence of wind speed. During very unstable conditions with low wind speed their horizontal shape is more circular (Priestley 1957; Wilczak and Tillman 1980). Within ramps, characteristic horizontal flow patterns are measured (Wilczak 1984; Weijers et al. 1994). The ramp interior is strongly convergent. Vertical vorticity is found on either side of the ramp, with opposite sign (Weijers et al. 1995).

In 1957, Priestley reported on an apparently fixed ratio of the space occupied by ascending and descend-

Current affiliation: KEMA Environmental Services, Arnhem, the Netherlands.

Corresponding author address: Prof. H. F. Vugts, Department of Meteorology, Vrije Universiteit, De Boelelaan 1085, 1081 HV Amsterdam, The Netherlands.
E-mail: vugh@geo.vu.nl

ing motions at several heights in the SL and under different stabilities of the atmosphere. The ascending fraction is assumed here to correspond to the presence of ramps (here denoted by γ, the intermittency factor). Taking the average of several experimental values for the SL (Priestley 1957; Frisch and Businger 1973; Khalsa 1980) as listed by Khalsa (1980), we find γ = 0.44. The remaining time consists of the accompanying downdrafts. Above the SL, plumes appear to merge together, forming the larger-scale thermal structures ("thermals") that can be found in the mixed layer (Young 1988).

The main objective of this study was to reveal the horizontal wind behavior within and nearby ramp structures. Furthermore, wind fields were decomposed into horizontal divergence, vertical vorticity, and deformation. To acquire the necessary dataset, a field experiment was performed with an array of five sensors on a horizontal scale of ~100 m. Ramps were then selected "by eye" based on their typical temperature trace. For the computation of the kinematic quantities during the passage of the ramps, the linear vector point function method (LVPF) was applied to the corresponding measurements of wind velocity (Zamora et al. 1987). The kinematic series of each selected ramp were block averaged into a number of bins. Ultimately, a composite was obtained by weighted averaging of the bin values. The method used here has been described by Wilczak (1984). Recent applications of this technique are demonstrated by Sikora and Young (1993, 1994), who estimated the horizontal distributions of fluxes and the perturbation wind fields within convective updrafts and downdrafts.

FIG. 1. Schematic diagram of the experimental site near the meteorological KNMI tower of Cabauw.

2. Experimental conditions and data analysis

a. Experiment

The data used were taken in May, June, and July 1992 near the meteorological tower (213 m) at the village of Cabauw (51°58′N, 4°55′E) in the Netherlands. For an extensive description of this location and the operation of the tower, we refer to Monna and van der Vliet (1987). The measurements took place on a flat square piece of grassland with its center about 225 m north of the Cabauw tower (for a schematic view see Fig. 1). One ultrasonic anemometer–thermometer (measuring height 31 m) was positioned at center C of the square area ABDE (sides 80 m). Four ultrasonic anemometers were used to measure horizontal and vertical wind velocity at a height of 13 m on the vertices of the experimental square. All five sonic anemometers were technically identical.

Anemometer outputs were sampled at 20 Hz. The measurements were performed during convective conditions ($-1 < z/L < -0.06$). In this study we used the data from 37 half-hour runs. Mean value and linear trends of each variable were removed to obtain the fluc-

tuating part. Much attention has been paid to the leveling and the flow modification of the sonic anemometer as well as to the error in the alignment. For a detailed description of these procedures, see Weijers et al. (1994).
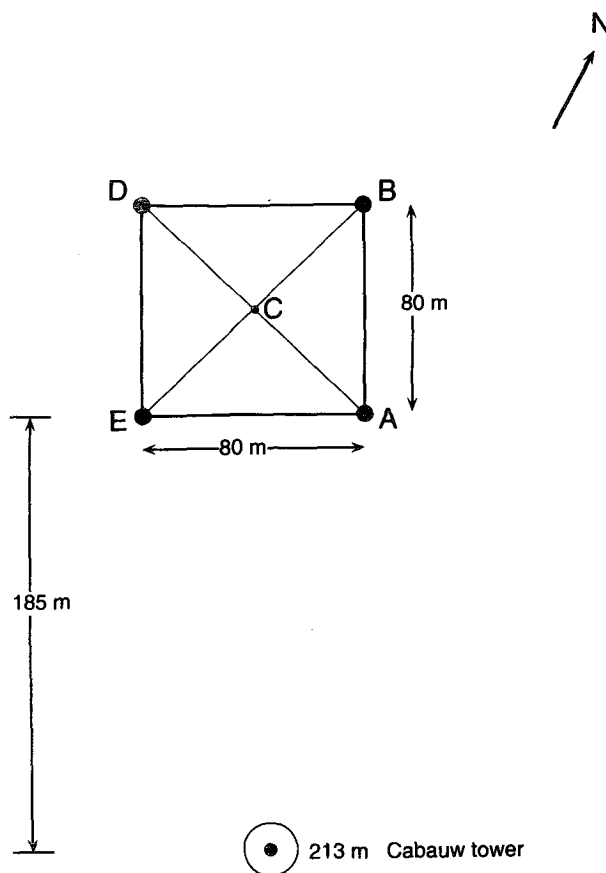
b. Definition and selection of ramps

After visual inspection, 47 ramps have been chosen. The selected structures had to be clearly defined, that is, sufficiently ramplike in appearance. An example can be seen in Fig. 2. Structures consisting of ramps merged together or overlapping the beginning or the end of a time series were excluded.

The length of a ramp is defined as the period starting when the turbulent temperature signal crosses through zero and ending at the sharp temperature jump at the upwind edge (indicated by arrows in Fig. 2). These moments were visually determined. The length of the accompanying downdraft is determined by the intermittency factor γ, such that the ratio of the ramp length to the total structure length (ramp plus downdraft) equals γ (=0.44). The period of the downdraft was thereafter divided into two halves, one preceding and
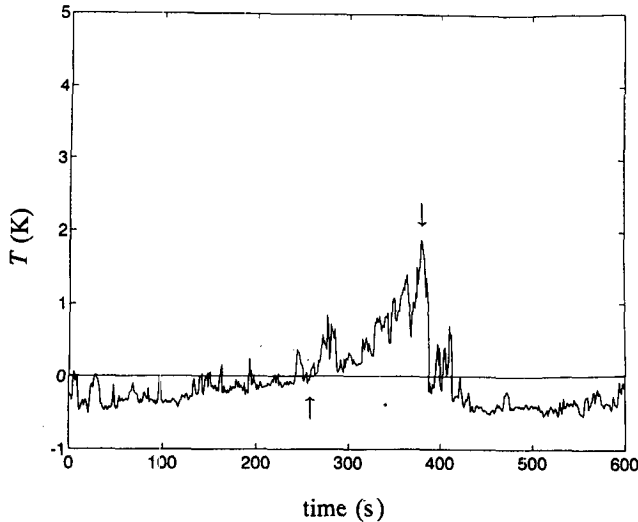
FIG. 2. Example of a ramp structure in a temperature time series registrated at the central mast C. Arrows denote the start and end of the ramp that will be used in the ensemble-averaging procedure.

one succeeding the ramp. Hence, each of these constitutes 28% of the total structure.

The local mean flow at the time of each selected ramp was estimated by averaging wind speed and wind direction (registrated at the 13-m masts) from 2 minutes before the start of the ramp until 2 minutes after the end of the ramp. Averaged over the 47 ramps we found a local mean wind speed ($\overline{u_{loc}}$) of 3.7 m s^{-1} (± 1.6 m s^{-1}). Multiplying the period between start and end of each ramp with u_{loc} gives an estimate of the (longitudinal) length in meters. On average, the ramp length appeared to be 236 m. Using $\gamma = 0.44$, the length of the entire structure was then 536 m. In the selection of ramps a minimum length was used to ensure that thermal activity is measured at the four outer masts. As a lower limit, 100 m seems appropriate, as it is comparable to the length of the diagonals in square ABDE.

Another criterion in the selection of ramps was that their propagation (estimated by the local mean wind direction) had to be approximately aligned (within $\pm 20°$) with one of the diagonals of the experimental square. This square area can then be divided into two triangles that are sampling different parts of a structure. For example, when the propagation direction of the ramp is approximately aligned with diagonal ACD in Fig. 1, we assume that triangle ABD is at the right-hand side, and triangle AED is at the left-hand side of the central axis of the ramp. Equally, the square area can be divided into triangles that have been traversed first (ABE) and second (DBE). Doing so, we can infer details on flow behavior within different portions of a ramp.

In the following, the relative positions of the triangles will be labeled F and S, indicating the first (up-

wind) and second (downwind) triangle to traverse, and R and L, indicating the triangles positioned at the right-hand and left-hand side of the structure when looking in the direction of the local mean flow. Sometimes these labels are used to denote the four outer masts. The label Sq refers to the square area.

c. Computation of the kinematic time series

After selecting the 47 ramp structures, kinematic variables could be calculated for the periods delineated by the ramps and accompanying downdrafts. For triangular arrays with three stations, a method that computes the kinematics must be based on the assumption of a linear wind field. Thus, when the wind field exhibits a large amount of nonlinear variation, we no longer have an accurate picture of the variations in the velocity field. With this limitation in mind, the four kinematic properties (horizontal divergence D, vertical vorticity ζ, and the deformation variables η_1 and η_2) were calculated by use of the linear vector point function method (LVPF) chosen for its computational efficiency, as we will later outline. For more details we refer to Zamora et al. (1987) and Doswell and Caracena (1988).

Using Taylor expansion with respect to some origin (x_0, y_0) of a fixed (Eulerian) reference frame (with x in the downstream direction), the linear velocity components u and v satisfy

$$u(x, y) = u(x_0, y_0) + \frac{\partial u}{\partial x}(x - x_0) + \frac{\partial u}{\partial y}(y - y_0),$$

and

$$v(x, y) = v(x_0, y_0) + \frac{\partial v}{\partial x}(x - x_0) + \frac{\partial v}{\partial y}(y - y_0).$$

$$(1)$$

The kinematic quantities are defined as usual (see, e.g., Bluestein 1992):

$$D = \frac{\partial u}{\partial x} + \frac{\partial v}{\partial y}, \quad \zeta = \frac{\partial v}{\partial x} - \frac{\partial u}{\partial y},$$

$$\eta_1 = \frac{\partial u}{\partial x} - \frac{\partial v}{\partial y}, \quad \eta_2 = \frac{\partial v}{\partial x} + \frac{\partial u}{\partial y}. \quad (2)$$

Substituting (2) in (1) yields

$$u(x, y) = u_0 + \frac{1}{2}(\eta_1 x + \eta_2 y + Dx - \zeta y)$$

and

$$v(x, y) = v_0 + \frac{1}{2}(-\eta_1 y + \eta_2 x + Dy + \zeta x), \quad (3)$$

where (u_0, v_0) is the wind speed in the origin of the square, which we have chosen in $(0, 0)$ to make the notation simpler. Having six unknowns in (3), denoted by the vector $\mathbf{D} = (2u_0, 2v_0, \eta_2, \eta_1, D, \zeta)$, we need three noncolinear wind measurements to solve the sys-

tem. Defining the observations at the three stations by the vector $\mathbf{U} = (u_1, v_1, u_2, v_2, u_3, v_3)$, we can write:

$$\mathbf{DX} = \mathbf{U}. \tag{4}$$

Here $\mathbf{X}$ is a 6×6 matrix determined by the network geometry. The kinematic magnitudes are then found by solving

$$\mathbf{D} = \mathbf{UX}^{-1}. \tag{5}$$

The inversion of the 6×6 matrix $\mathbf{X}$ has to be done only once for a fixed triangle. In practice for each case for which wind observations were done at the three stations, we multiply them with the stored matrix $\mathbf{X}^{-1}$ to obtain the kinematic variables.

From the coordinate-dependent quantities η_1 and η_2, coordinate-independent deformation quantities can be inferred, which are defined as follows. Consider the evolution of a "star" made of material line segments through a given point. One defines the deformation axes as the directions of the line segments that will undergo, in the immediate future, extremal change of length (maximal or minimal dilatation or contraction). These axes are always mutually perpendicular (because the velocity field is differentiable). See Fig. 3 for an example in an axisymmetric shear field. Here $L(1)$ and $R(1)$ are the material line segments aligned with the axis of dilatation (d) and contraction (c); $L(2)$ and $R(2)$ are the same lines after deformation. The angle of the deformation axes and the x axis is

$$\theta_d = \frac{1}{2} \arctan \frac{\eta_2}{\eta_1} \tag{6}$$

(modulo $\pi/2$). In this study, the x axis was aligned with the ramp-propagation velocity. The coordinate-independent deformation quantities are defined by considering the evolution of a material rectangle that is initially aligned with the deformation axes (Fig. 3). The angular velocity with which the rectangle rotates (both sides always rotate with the same rate, so that the rectangle remains a rectangle) appears to be $\zeta/2$. The rate of change of the area of the rectangle (relative to the original area) equals the divergence D. Finally, the deformation $|\eta|$ is defined as the rate of change of the proportion between the two sides (relative to the original proportion), for this one has

$$|\eta| = \sqrt{\eta_1^2 + \eta_2^2}. \tag{7}$$

d. Ensemble averaging

The method of constructing ensemble composites after block (or bin) averaging was presented by Wilczak (1984). We now briefly describe the mathematical details and practical application. First, the various velocity and kinematic time series belonging to the 47 ramps and the corresponding series of temperature and vertical velocity were averaged into 32 blocks, usually re-

ferred to as bins. To account for the varying lengths of each ramp, the start was always chosen in bin 10 and the end in bin 23. Hence, the ratio of ramp length to total length is $14/32 = 0.44$ $(= \gamma)$. In case of a ramp i, the jth bin average of a variable D_{ijk} is given by

$$\bar{D}_{ij}^{(bin)} = \frac{1}{n_i} \sum_{k=1}^{n_i} D_{ijk}. \tag{8}$$

Here, D_{ijk} is the kth measurement within bin j. Let l_i be the number of measurements during ramp i; then the rounded value of n_i $(= l_i/14)$ is the number of points in a bin belonging to this ramp. The duration of a bin varied between 2 and 10 s. The average number of seconds in a bin was 4.4 s and corresponds to a length of about 17 m.

The bin averages may contain a low-frequency component, that is, random low-frequency turbulence superimposed on the activity of the ramp and surrounding downdrafts. We can distinguish the ramp from the random turbulence by forming a composite of the $m = 47$ selected ramps. Because the ramps are of different lengths, each will be weighted according to its length. The composite value of the jth bin can then be computed by

$$\bar{D}_j^{(ens)} = \frac{\sum\limits_{i=1}^{m} l_i \bar{D}_{ij}^{(bin)}}{\sum\limits_{i=1}^{m} l_i}. \tag{9}$$

Using $l_i/14 = n_i$ and Eq. (8), we rewrite this as

$$\bar{D}_j^{(ens)} = \frac{\sum\limits_{i=1}^{m} \sum\limits_{k=1}^{n_i} D_{ijk}}{\sum\limits_{i=1}^{m} n_i}. \tag{10}$$

Hence, the ensemble averages can be calculated directly from the instantaneous measurements.

The deviation of the jth bin average (weighted by the length of ramp i) from the jth ensemble average is

$$\delta D_{ij} = \frac{l_i}{\sum\limits_{i=1}^{m} l_i} \bar{D}_{ij}^{(bin)} - \bar{D}_j^{(ens)}, \tag{11}$$

leading to the definition of the standard deviation of the (weighted) bin averages:

$$\sigma_j^{(ens)} = \frac{1}{\sqrt{m(m-1)}} [\sum\limits_{i=1}^{m} (\delta D_{ij})^2]^{1/2}. \tag{12}$$

For computational reasons we rewrite Eq. (11) as

$$\delta D_{ij} = \frac{n_i}{\sum\limits_{i=1}^{m} n_i} \bar{D}_{ij}^{(bin)} - \bar{D}_j^{(ens)} = \frac{\sum\limits_{k=1}^{n_i} D_{ijk}}{\sum\limits_{i=1}^{m} n_i} - \bar{D}_j^{(ens)}. \tag{13}$$
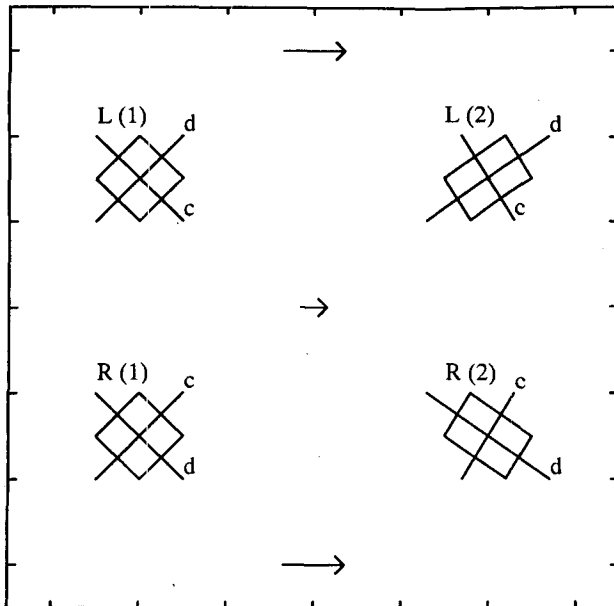
FIG. 3. Material line segments before [L(1), R(1)] and after [L(2), R(2)] deformation. The direction and magnitude of the flow field is indicated by the arrows.

3. Results

Ensemble averages (using the 47 selected ramps) of temperature, horizontal and vertical wind speed, horizontal divergence, vertical vorticity, resultant deformation, and dilatation axis were calculated. The kinematic quantities were estimated for each of the triangular areas F(irst), S(econd), R(ight), and L(eft). For the entire square area they were found by summing the ensemble averages of D, ζ, η_1, and η_2 of two oppositely located triangles and dividing by 2.

The central-mast temperature was measured at a height of 31 m. When a microfront reaches this mast with an assumed tilt of 45° (Antonia et al. 1979), less than 8% of the ramp (average length is 236 m) is still in the F triangle at the height of the wind speed measurements (13 m). The average local mean wind speed, $\overline{u_{loc}}$, was 3.7 m s^{-1}. Hence, the occurrence of the microfrontal temperature maximum at 31 m is believed to precede the maximum at 13 m with approximately the duration of one bin (4–5 s).

a. Temperature, horizontal velocity, and vertical velocity

In Fig. 4 are shown the ensemble averages of the temperature at mast C (T_C), the vertical velocity at mast C (w_C), and the vertical velocities (w_F, w_S) at the masts that are assumed to detect the passage of the ramps first and last in the experimental square (along one of the diagonals). Also, the corresponding averages of the alongwind and crosswind velocity compo-
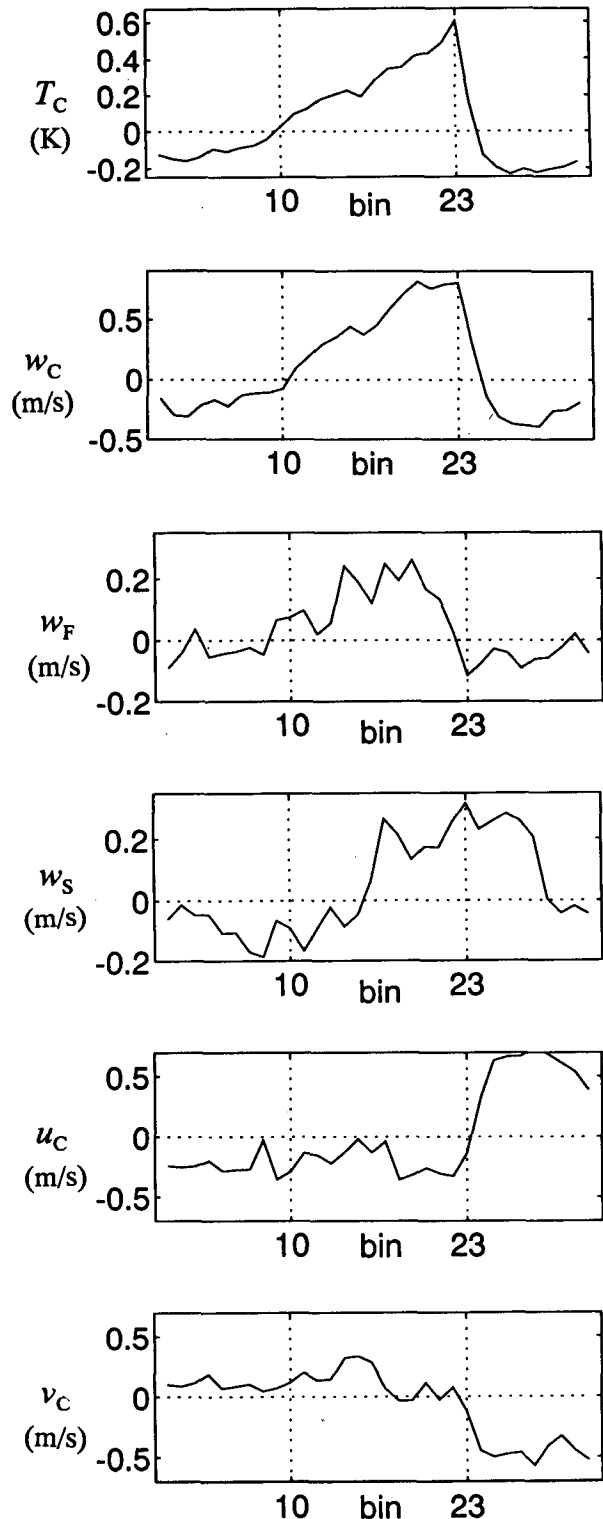

FIG. 4. The ensemble averages (over 47 ramps) of the turbulent perturbations of the temperature (T_C), vertical wind speed (w_C), both measured at mast C, of the vertical wind speed measured at mast F and S (w_F and w_S), and of the horizontal wind components (u_C, v_C) measured at mast C. Standard deviations [derived from Eq. (12)] are 0.03 K for the temperature, 0.08 m s^{-1} for the vertical velocities, and 0.17 m s^{-1} for the horizontal wind components.

FIG. 5. Horizontal wind field for the 32 bins after the ensemble-averaging procedure. The propagation direction is from left to right. The arrows are based at vertices and center of the experimental square.

nents registrated at mast C (u_C, v_C) are shown. The vertical dotted lines mark the beginning (bin 10) and end (bin 23) of the ensemble-averaged ramp structure.

As expected, a sawtooth pattern appears in the trace of T_C. The similarity between T_C and w_C is obvious: warmer air within the ramp ascends and is surrounded by colder descending air. However, the maximum ver-tical velocity seems to occur somewhat earlier than the upwind sharp temperature drop (bin 23), as observed earlier by Antonia and Chambers (1978). After the vertical velocity has reached its maximum, it takes 2 to 3 bins to fall down to zero. During this time the transport of heat from below still continues, causing the maximum in temperature to appear somewhat later.
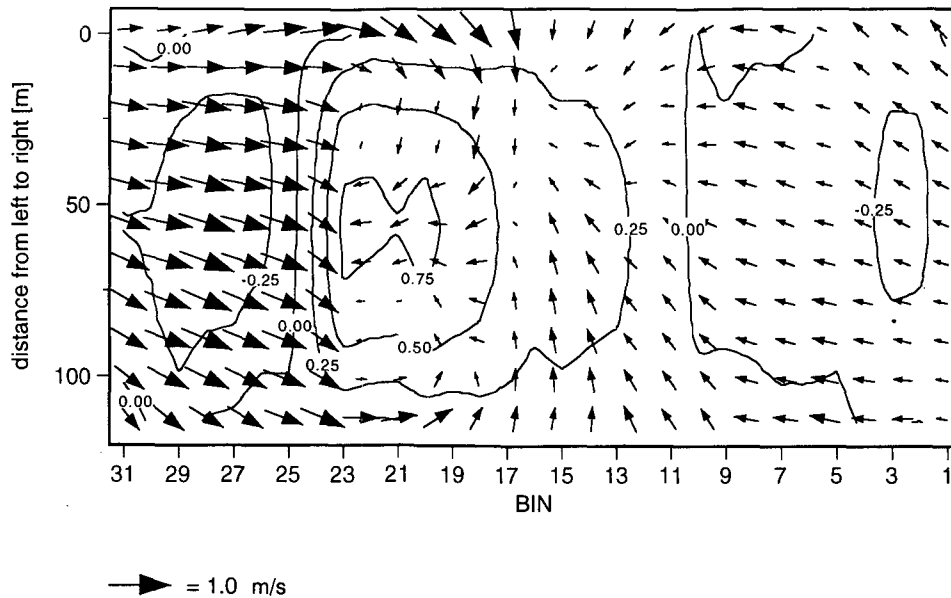
FIG. 6. Interpolated wind field corresponding to the ensemble-averaged ramp structure. Contours are w (in m s^{-1}). The interpolation uses the results of the three crosswind stations. For explanation see text.

In the ensemble averages of w_F and w_S, the typical ramp shape has largely disappeared. The ensemble traces are more noisy and have smaller amplitudes than in the case of w_C. This is not surprising as the averaging procedure has been based on the temperature recordings of mast C. However, thermal activity is still noticeable in the F and S triangles appearing earliest in the w_F trace and latest in the w_S trace, as expected.

This lag can be used to estimate the translation speed of the ensemble-averaged ramp structure while passing the experimental square. The zero crossing marking the end of the composite ramp as measured at mast S is 8 bins behind the corresponding zero at mast F. Using the zero crossings (at masts F and S) marking the beginning of the ensemble-averaged ramp the same difference is found, suggesting that no change in shape of the average plume occurred during passage. With an average bin duration of 4.4 s and a distance of 113 m between mast F and mast S, the velocity for the (ensemble-averaged) ramp is 3.2 m s^{-1}. This is 80% of the average background wind speed at 13 m (derived from the geometric means of the Cabauw-tower half-hour averages at 10 and 20 m). An accuracy error of ±1 bin results in an error range of 2.9–3.7 m s^{-1}, only just comparable to $\overline{u_{loc}}$ (3.7 ± 1.6 m s^{-1}).

Looking at the behavior of the turbulent horizontal wind components at mast C, we note that the longitudinal component u_C is predominantly negative within the boundaries of the ramp, hence against the direction of the mean local wind. This is due to the upward transport of slower air. Also, u_C increases just ahead of the temperature jump and becomes strongly positive after the microfront has passed. In the frame of reference of

the sonic anemometers the ramp is an area where the wind speed is lower than the background wind. The lateral velocity component v_C is slightly positive inside the ramp and negative within the succeeding downdraft. It suggests that the center of the ensemble-averaged structure is somewhat to the left of the presupposed passage along the diagonal of the square. In the latter case, v_C is expected to be relatively inactive.

b. Flow fields

Details on the horizontal wind field within and near ramp structures have been derived from the ensemble averages of the perturbation wind components u and v recorded at the five masts. Changes in wind speed and wind direction during passage of the (ensemble-averaged) ramp are shown in Fig. 5. Arrows (one for each mast) depict the vectorial sum of the u and v components. The propagation is from left to right.

The time behavior at all stations shows the effect of the passage of thermal structures in our array. Though measured at a different height, the velocity at the square's center does not behave inconsistently. It is interesting to see that the wind directions at the crosswind locations R and L gradually turn from left to right during bin 11 to 22, thereby inducing horizontal convergence by systematically pointing to the central area of the ramp. The presence of circulations is suggested at both halves of the ramp (with opposite sign), especially during the bins 18 to 22. It is also demonstrated (see, e.g., bin 5 to 18) that the path of the ensemble-averaged ramp was somewhat left of the square's center, as indicated earlier.
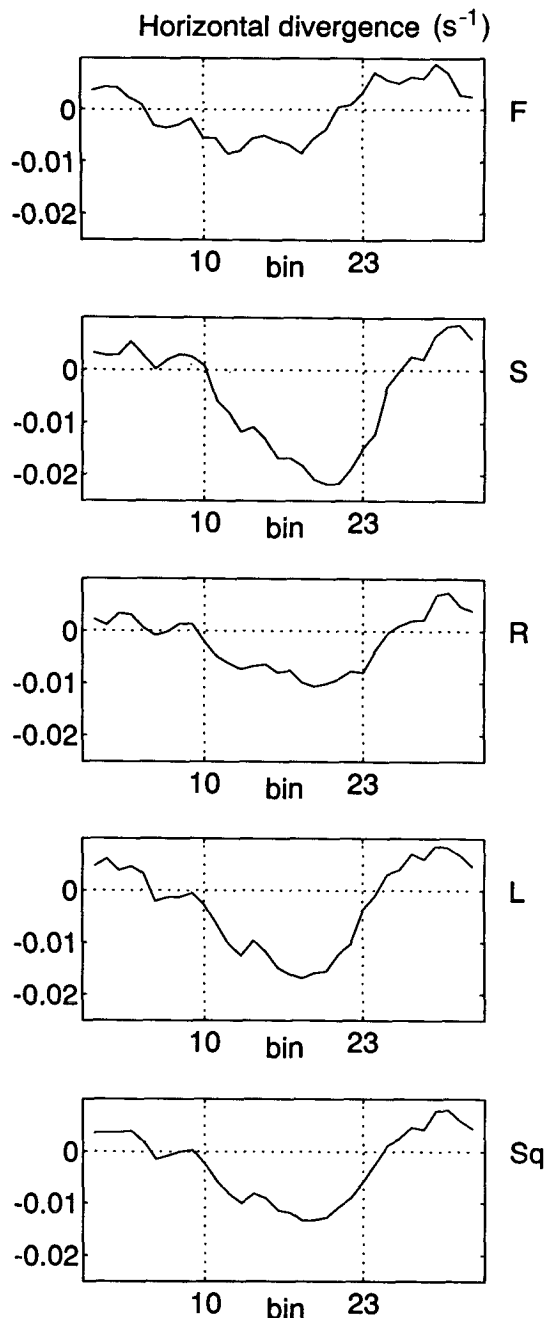
Horizontal divergence (s^{-1})

FIG. 7. The ensemble averages of horizontal divergence in the four triangles and for the entire square (Sq). Standard deviation is 0.003 s^{-1}. Terms F and S denote the first and second triangle entered by the ramp; R and L are the triangles assumed to be located in the right and left part of the ramp structure when looking in the direction of propagation.

A horizontal cross section of the ensemble-averaged ramp is given in Fig. 6, produced by use of the measurements at the three crosswind stations. The flow pattern between the wind sensors has been estimated by interpolation of the ensemble-averaged wind compo-

nents using the formula of Lagrange (Daley 1991). Also given are contours of w (in m s^{-1}).

Here the 31-m data at the central mast has been combined with the 13-m data at the two lateral masts. We have thus assumed that the structure of the perturbation horizontal wind field around the plume is the same at both heights. In order to correct for the likely fact that the plume is tilted forward due the vertical shear of the mean wind, we have shifted the bin-averaged wind vector at the central mast (31 m) by one bin compared to the bin-averaged wind vector at the lateral masts (13 m). More specifically, the wind vector at the central mast in bin 1 is shifted to bin 2, etc., in accordance with the earlier finding that a lag of one bin exist between the measurements at 31 m and those at 13 m.

Clearly, the wind field is divergent on either side of the ramp (bin 1 to 9 and bin 25 to 32) combined with relatively weak downward movements. A convergent field exists within the ramp, being stronger in absolute magnitude. The area of upward movement covers a fairly large part within the ramp. The picture suggests a clear lateral inflow of environmental air, which agrees with the findings of Wilczak (1984). Such an inflow causes small areas of upward fluxes of horizontal momentum at places where the environmental air reaches the edges of the plume (Williams and Hacker 1992).

Obviously, air decelerates within the ramp boundaries and accelerates immediately after the microfront. In the frame of reference moving with the ramp the average orientation of the wind in the accompanying downdrafts is always directed toward the position of the ramp. The turbulent wind speed perturbations measured in the preceding downdraft are roughly half as large (taken absolutely) as those observed in the succeeding downdraft.
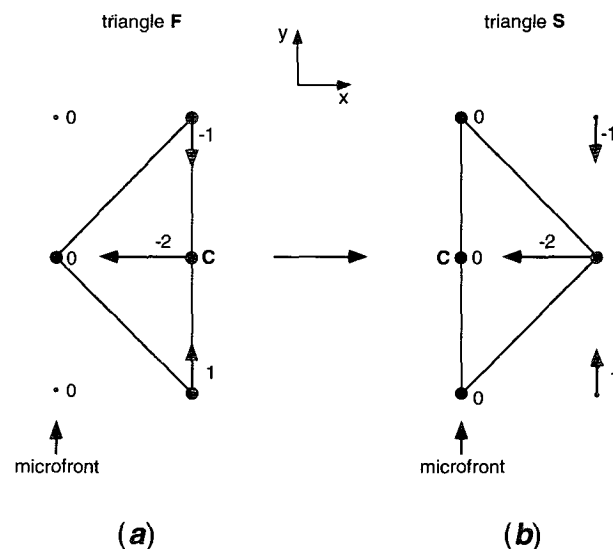

FIG. 8. The locations of the first (a) and second (b) triangle in the nonlinear horizontal wind field of a simplified ramp.
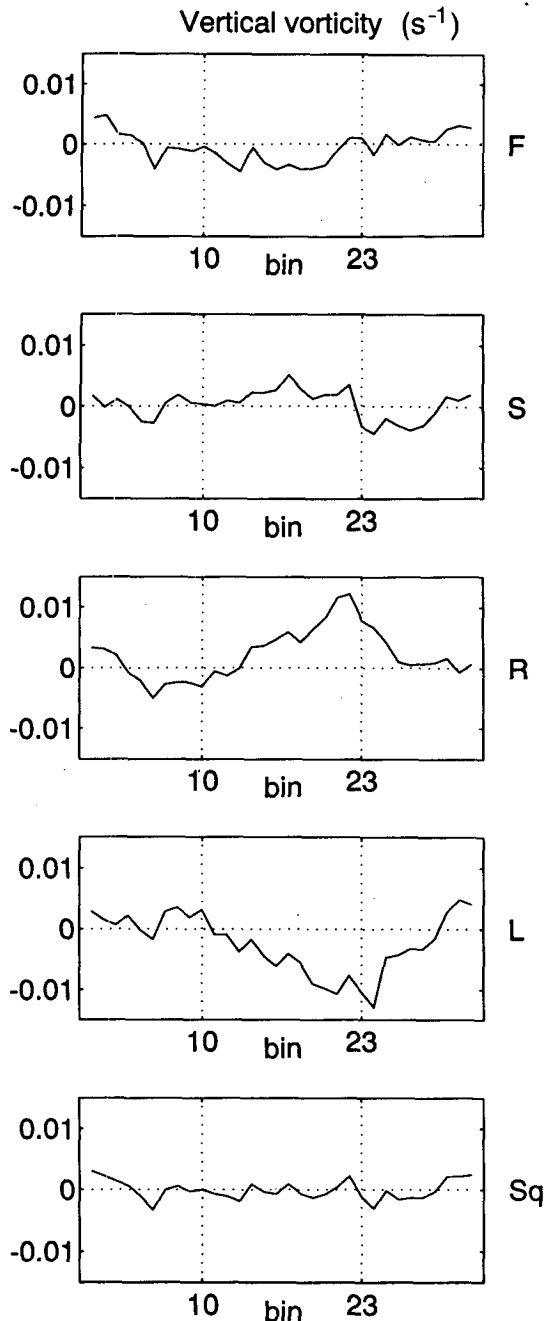
Vertical vorticity (s⁻¹)

FIG. 9. As Fig. 7 but now for the vertical vorticity. Standard deviation is 0.003 s⁻¹.

c. Divergence and vorticity

The ensemble-averaging procedure for the wind speed variables at the four outer masts revealed certain flow patterns in and around the ramp structure. We can quantify such flows by estimating their (ensemble-averaged) kinematic properties.

As shown in Fig. 7, convergence prevails in all four triangular areas. The maximum convergence in

triangle S has been attained somewhat before the arrival of the microfront at C, coinciding with the maximum of w_C. We further note a difference of a factor 2–3 in the divergence signals measured in the triangles F and S. Most likely, this is due to the violation of the assumption that the wind field is linear. Evidence of nonlinearity is already given in Figs. 5 and 6. The geometrical reason for this bias error is associated with the orientation of these triangles with respect to the nonlinear wind field. To illustrate this, let the u, v components of a hypothetical nonlinear wind field be given in Figs. 8a–b ($\partial^2 u/\partial y \partial x \neq 0$). This horizontal wind field is supposed to be representative (to some extent) for the interior of a (average) ramp structure. Also drawn are the hypothetical locations of the triangles F (Fig. 8a) and S (Fig. 8b). The propagation is from left to right. It is assumed here that the wind field remains the same during passage of the experimental square area. In Fig. 8a the microfront just enters triangle F. At that moment the horizontal divergence estimated in F by the LVPF method is -0.018 s⁻¹. When the microfront arrives at the central mast C (Fig. 8b), the horizontal divergence in S is twice the value found earlier in F.

The triangles R and L are laterally symmetric with respect to the x axis. Hence, in a symmetric wind field the divergence estimates must be the same (and irrespective of the fact whether the wind field is nonlinear or not). However, this is not the case in Fig. 7. Another error source must be present. It is likely that the difference in divergence magnitudes between triangles R and L is due to the earlier observation that, on average, measurements were biased to the right-hand side of the ramp.

In the case of vertical vorticity (Fig. 9), significant values have been found in the triangles R and L. As already suggested in Figs. 5 and 6, an area of positive vorticity exists in the right half of the ramp (with respect to the direction of propagation), with a counterpart of negative vorticity in the left half. For the entire square area (picture denoted by Sq), vertical vorticity is practically zero. The existence of some kind of circulation within or at the flanks of a ramp was noticed earlier (Wilczak 1984; Williams and Hacker 1992; Weijers et al. 1994).

To understand this, first consider the ramp as an object of limited horizontal extent, being slower than the background wind. Therefore, air at the flanks moves faster, which creates shear in the crosswind direction such that $\partial u/\partial y < 0$ at the right-hand side and $\partial u/\partial y > 0$ at the left-hand side of the ramp. Hence, vertical vorticity is found in these areas according to Eq. (2) ($\zeta \approx -\partial u/\partial y$).

To explain the possible development of the wind field within ramps, two phenomena that play a role in the generation or intensification of horizontal circulations must be considered. To this purpose, we employ
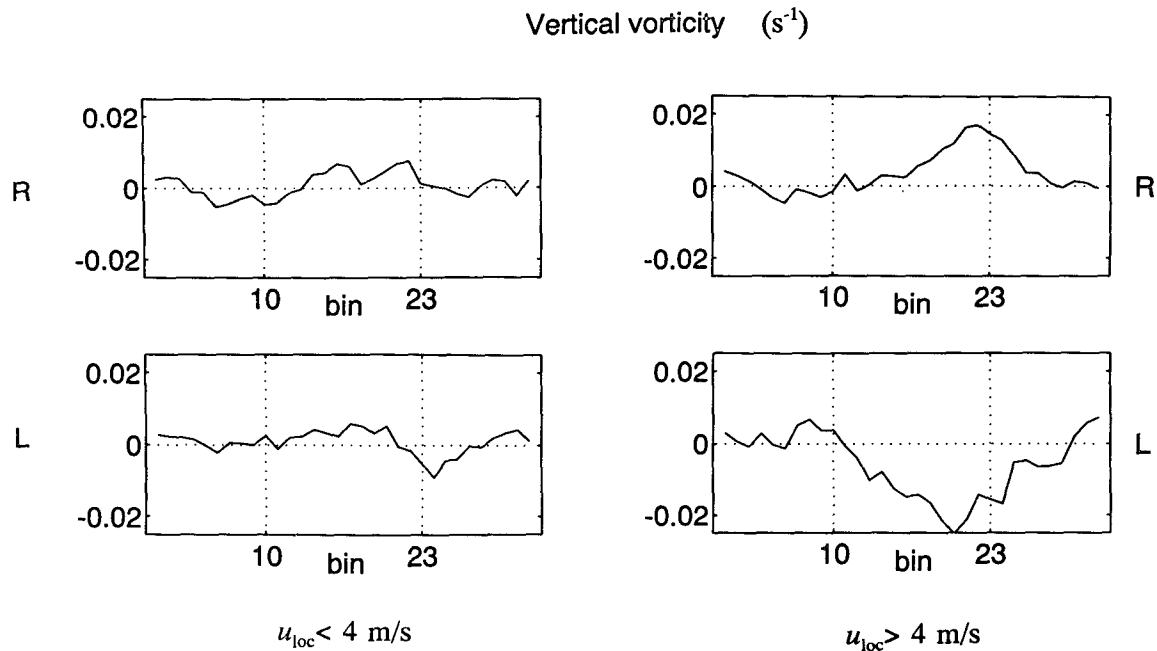
Vertical vorticity   (s⁻¹)

FIG. 10. Ensemble averages of vertical vorticity in the triangles R and L for ramps with a mean local wind speed (u_{loc}) of less than 4 m s^{-1} (left pictures) and larger than 4 m s^{-1} (right pictures).

the equation for the rate of change of the vertical component of the vorticity (Dutton 1986):

$$\frac{d\zeta}{dt} = \zeta \frac{\partial w}{\partial z} - \left(\frac{\partial w}{\partial x} \frac{\partial v}{\partial z} - \frac{\partial w}{\partial y} \frac{\partial u}{\partial z} \right). \qquad (14)$$

The first process to be discussed is the tilting of environmental horizontal vorticity into the vertical [term between brackets in Eq. (14)]. Horizontal vorticity of environmental air is due to vertical wind shear. Linearizing the vertical vorticity equation yields

$$\frac{d\zeta}{dt} = \frac{dU}{dz} \frac{\partial w}{\partial y}. \qquad (15)$$

Assuming $dU/dz > 0$, which is true on average, and measuring the largest positive vertical velocities in the central region of the ramp, tilting generates positive vertical vorticity at the right flank of the ramp (here $\partial w / \partial y > 0$) and negative vorticity at its left flank ($\partial w / \partial y < 0$). This effect does not only enhance existing circulations but can also create circulations in both halves of the ramps. Similar circulations (but on a different scale) arise when thunderstorms grow in environments with unidirectional shear (Rotunno and Klemp 1985; Lilly 1986; Klemp 1987).

The second process is stretching [the first term on the right-hand side in Eq. (14)]. Air within a ramp accelerates upward due to buoyancy at its base. Hence, $\partial w / \partial z$ is positive in the central region of the ramp. The stretching term will therefore intensify already existing rotations. Again, this will only be true on average since

air in the ramp is rather turbulent and vertical velocity may be downward in some random spots within the ramps.

It is interesting to study the role of the background wind speed. To this purpose, the 47 selected structures were further divided into two subsets: one consisting of ramps with a mean local wind speed less than 4 m s^{-1} and a set containing the ramps with a mean local wind speed larger than 4 m s^{-1}; the number of structures in these sets were 23 and 24, respectively. Ensemble averaging was done for both sets. Results are displayed in Fig. 10 for the vertical vorticity within the triangles R and L. It appears that vertical vorticity is only measurable when there is sufficient background wind. The first reason for this may be the tilting process discussed previously. As indicated by Eq. (15), a larger wind shear induces more vertical vorticity. A second possibility is that the crosswind dimensions of the ramps have become much larger than 100 m for light winds and that the array does not measure the circulations at the flanks. Horizontal divergence in R and L under low wind speed conditions (not shown) is of the same magnitude as in Fig. 10. Under these conditions this signal may be the result from both a lateral inflow and an inflow from the "front" and "back" of the ramp.

d. Resultant deformation and dilatation axis

The ensemble averages of the resultant deformation and the dilatation axis are given in Fig. 11 and Fig. 12, respectively. From Fig. 11 (triangles F and S) it is de-
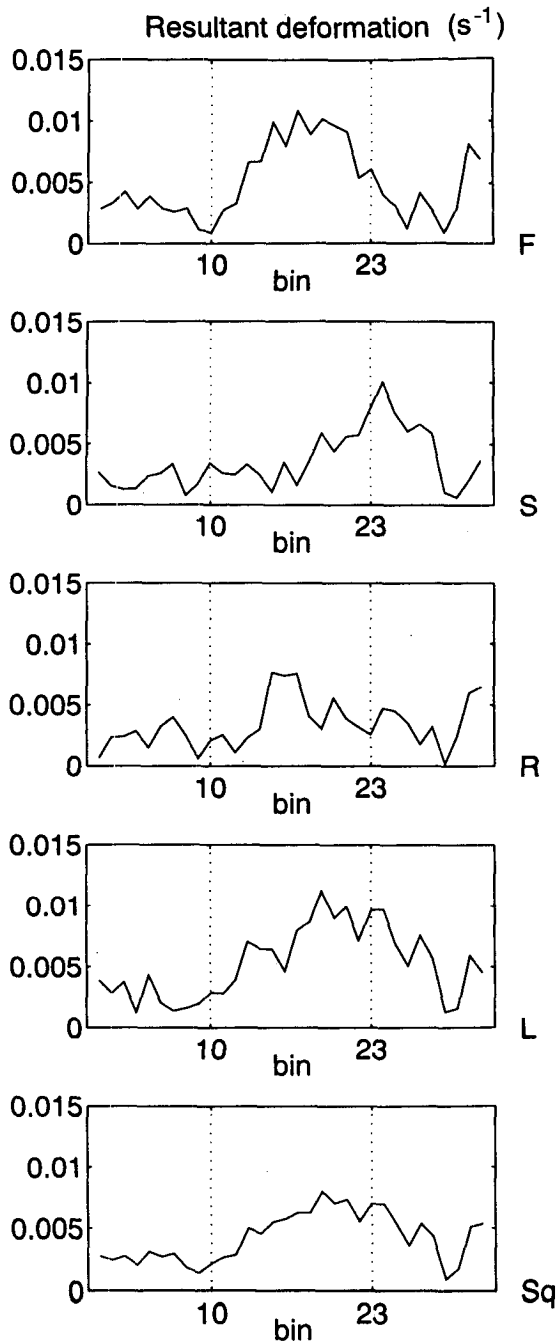
Resultant deformation (s⁻¹)

FIG. 11. As in Fig. 7, but for the resultant deformation.
Standard deviation is 0.003 s⁻¹.

dicular to the direction of the background wind. Hence, in the region around the microfront, contraction occurs parallel to the propagation direction, being strongest in the succeeding downdraft. In this region, the cooler air flows against the warmer air within the structure, causing air to circulate around the microfront. The opposite behavior of θ_d at the triangles R and L illustrates the symmetry of the ramps. Deformation is caused by the
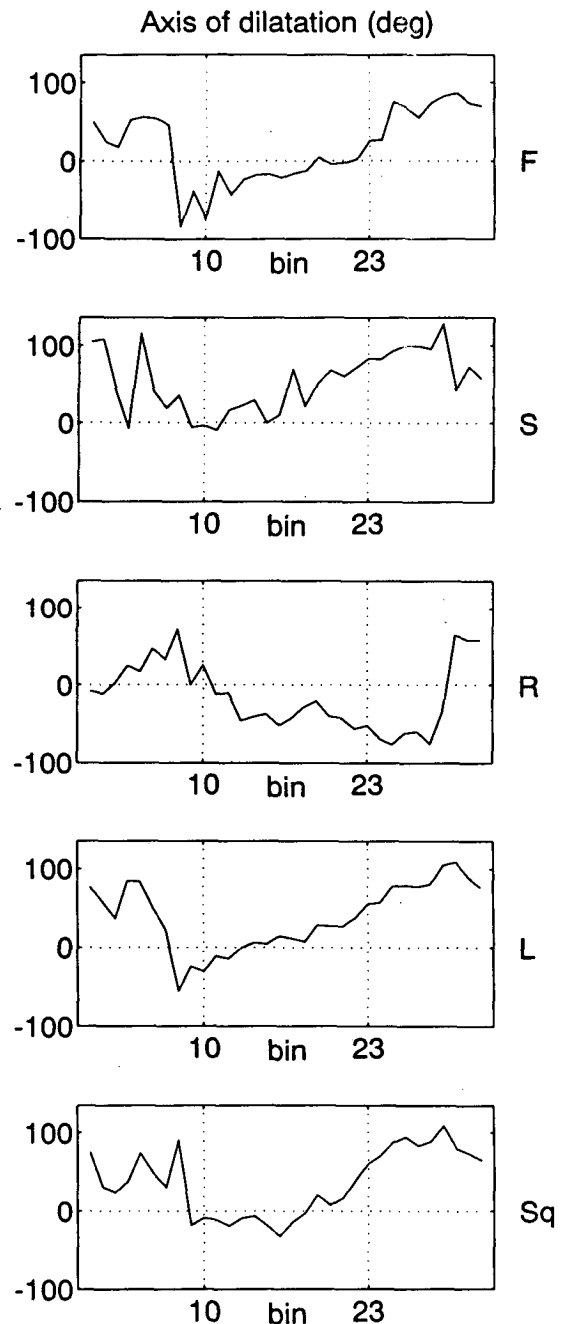
Axis of dilatation (deg)

FIG. 12. As in Fig. 7, but for the axis of dilatation.
Standard deviation is 8°.

duced that deformation is present in and near the ramp structure. During the first part of the ramp (see Fig. 12, picture Sq), the angle of the axis of dilatation, θ_d, is around 0°. This means that dilatation is measured in the direction of the background wind. However, in the region closer to the microfront the direction of maximum dilatation changes, ultimately making an angle perpen-

higher wind speed at the flanks of the ramp in a way illustrated by Fig. 3.

4. Conclusions and summary

Patterns in the horizontal circulation field within ramp structures were investigated. The analysis consisted of a combination of conditional sampling, block averaging, and ensemble averaging (Wilczak 1984). The method performed well on data of turbulent temperature and wind components belonging to 47 selected ramps. These were measured with five sonic anemometers at the vertices and the center of a square area (sides 80 m). Ensemble averages were calculated for temperature, wind speed, horizontal divergence, vertical vorticity, and deformation. The kinematic variables were estimated by use of the Linear Vector Point Function method (Zamora et al. 1987).

An apparent similarity between the behavior of vertical velocity and temperature was found: both have a sawtooth appearance. However, the maximum vertical velocity occurs 8 to 15 s earlier than the maximum temperature at the microfront. The longitudinal wind speed within the ramp is predominantly negative but becomes strongly positive after the microfront.

By tracing the thermal activity within the array of stations, the translation velocity of the ensemble-averaged ramp could be determined: it was about 20% lower then the average background wind speed (at the measurement height of 13 m).

The horizontal wind field within the ensemble-averaged ramp was estimated by interpolating the (ensemble-averaged) turbulent wind speed variables of the three crosswind stations in our array. As expected, the wind field in the ramp area is convergent. Like vertical velocity, the maximum convergence precedes the upwind microfrontal edge. The divergence within the accompanying downdrafts is relatively weak.

Circulations of opposite sign develop at the right and left flank of a ramp. These circulations will gain from the stretching of vertical vorticity within the ramp and from the tilting of environmental horizontal vorticity into the vertical direction. The strength of the background wind might play a role in the intensification of these rotations. The vortex pair disappears (like the typical ramp behavior) when the background wind becomes negligible. The lateral inflow does not depend on the existence of the rotations at the flanks because it would continue to be important when the background wind goes to zero. The thermal structure would then have as much inflow from the "sides" as from the "front" and the "back."

Within the ramp structure, dilatation of air is initially measured along the direction of propagation. This gradually changes into contraction of air, with a maximum somewhat beyond the microfront.

REFERENCES

Antonia, R. A., and A. J. Chambers, 1978: Note on temperature ramp structure in the marine surface layer. *Bound.-Layer Meteor.*, **15**, 347–355.

——, ——, C. A. Friehe, and C. W. Van Atta, 1979: Temperature ramps in the atmospheric surface layer. *J. Atmos. Sci.*, **36**, 99–108.

Bluestein, H. B., 1992: *Synoptic-Dynamic Meteorology in Midlatitudes.* Vol. 1: *Principles of Kinematics and Dynamics.* Oxford University Press, 431 pp.

Davison, D. S., 1974: The translational velocity of convective plumes. *Quart. J. Roy. Meteor. Soc.*, **100**, 572–592.

Daley, R., 1991: *Atmospheric Data Analysis.* Cambridge University Press, 457 pp.

Doswell, C. A., III, and F. Caracena, 1988: Derivative estimation from marginally sampled vector point functions. *J. Atmos. Sci.*, **45**, 242–253.

Dutton, J. A., 1986: *The Ceaseless Wind, an Introduction to the Theory of Atmospheric Motion.* Dover, 617 pp.

Frisch, A. S., and J. A. Businger, 1973: A study of convective elements in the atmospheric surface layer. *Bound.-Layer Meteor.*, **3**, 301–328.

Kaimal, J. C., 1974: Translation speed of convective plumes in the atmospheric surface layer. *Quart. J. Roy. Meteor. Soc.*, **100**, 46–52.

——, and J. A. Businger, 1970: Case studies of a convective plume and a dust devil. *J. Appl. Meteor.*, **9**, 612–620.

Khalsa, S. J. S., 1980: Surface-layer intermittency investigated with conditional sampling. *Bound.-Layer Meteor.*, **19**, 135–153.

Klemp, J. B., 1987: Dynamics of tornadic thunderstorms. *Ann. Rev. Fluid Mech.*, **19**, 369–402.

Lilly, D. K., 1986: The structure, energetics and propagation of rotating convective storms. Part I: Energy exchange with the mean flow. *J. Atmos. Sci.*, **43**, 113–140.

Monna, W. A. A., and J. G. van der Vliet, 1987: Facilities for research and weather observations on the 213 m tower at Cabauw and at remote locations. Scientific Report WR no. 87-5, KNMI, the Netherlands, 27 pp.

Phong-Anant, D., A. J. Chambers, and R. A. Antonia, 1981: Spatial coherence to temperature fluctuations in the atmospheric surface layer. *Bound.-Layer Meteor.*, **21**, 465–475.

Priestley, C. H. B., 1957: Convection from the earth's surface. *Proc. Roy. Soc. A.*, **238**, 287–304.

Rotunno, R., and J. Klemp, 1985: On the rotation and propagation of simulated supercell thunderstorms. *J. Atmos. Sci.*, **42**, 271–292.

Sikora, T. D., and G. S. Young, 1993: Observations of planview flux patterns within convective structures of the marine atmospheric surface layer. *Bound.-Layer Meteor.*, **65**, 273–288.

——, and ——, 1994: Observation and applications of the horizontal perturbation wind field within convective structures of the marine atmospheric surface layer (Research Note). *Bound.-Layer Meteor.*, **68**, 419–426.

Taylor, R. J., 1958: Thermal structures in the lowest layer of the atmosphere. *Aust. J. Phys.*, **11**, 168–176.

Weijers, E. P., A. van Delden, and H. F. Vugts, 1994: Kinematic estimates within surface-layer thermal structures. *Bound.-Layer Meteor.*, **67**, 145–160.

——, ——, ——, and A. G. C. A. Meesters, 1995: Characteristics of convective turbulence in the surface layer investigated by principal component analysis. *J. Appl. Meteor.,* **34,** 528–541.

Wilczak, J. M., 1984: Large-scale eddies in the unstably stratified atmospheric surface layer. Part I: Velocity and temperature structure. *J. Atmos. Sci.,* **41,** 3537–3550.

——, and J. E. Tillman, 1980: The three-dimensional structure of convection in the atmospheric surface layer. *J. Atmos. Sci.,* **37,** 2424–2443.

Williams, A. G., and J. M. Hacker, 1992: The composite shape and structure of coherent eddies in the convective boundary layer. *Bound.-Layer Meteor.,* **61,** 213–246.

Young, G. S., 1988: Convection in the atmospheric boundary layer. *Earth Sci. Rev.,* **25,** 179–198.

Zamora, R. J., M. A. Shapiro, and C. A. Doswell III, 1987: The diagnosis of upper tropospheric divergence and ageostrophic wind using profiler wind observations. *Mon. Wea. Rev.,* **115,** 871–884.